Terrestrial Observations from NOAA Operational Satellites

H. YATES, A. STRONG, D. MCGINNIS, JR., D. TARPLEY

Important applications to oceanography, hydrology, and agriculture have been developed from operational satellites of the National Oceanic and Atmospheric Administration and are currently expanding rapidly. Areas of interest involving the oceans include sea surface temperature, ocean currents, and ocean color. Satellites can monitor various changing hydrological phenomena, including regional and global snow cover, river and sea ice extent, and areas of global inundation. Agriculturally important quantities derived from operational satellite observations include precipitation, daily temperature extremes, canopy temperatures, insolation, and snow cover. This overview describes the current status of each area.

ALTHOUGH MEETING THE DEMANDS OF WEATHER FORECASTING was the original justification for the operational satellites of the National Oceanic and Atmospheric Administration (NOAA), and the meteorologist remains the predominant customer today, important applications in oceanography, hydrology, and agriculture have been developed and are expanding rapidly. The preoccupation with meteorology is in large part a consequence of the fact that the atmosphere is the first thing one sees from space. To observe surface features one must look through the atmosphere, and for most such observations our essential mantle of gas, haze, and clouds is a nuisance and a formidable source of masking and interference. The valuable data available for terrestrial monitoring, however, have prompted the development of effective methods correcting for the atmospheric interference.

The Oceans

NOAA satellites provide sea surface temperature (SST) data weekly on a 50- to 100-km grid with a mean bias of only +0.2°C and a standard deviation about this bias of 0.6°C, based on matchups with drifting buoys (*1*). The monthly mean product that accumulates typically 2 million of these observations globally into a grid of 2.5° of latitude and longitude has yielded root-mean-square differences of less than 0.3°C since late 1983, if as few as 10 of an average of 500 retrievals at each grid location can be accepted as independent (*2*). Precision has always been good, so gradient data have been in use for some years, but atmospheric water vapor and aerosols require a correction. It has been possible to make this correction to the requisite accuracy only in the past 2 years by using multiple infrared channels on the NOAA advanced very high resolution radiometer (AVHRR).

With the development of multichannel SST (MCSST) algorithms by NOAA's National Environmental Satellite, Data, and Information Service (NESDIS), global SST mapping has become routine (*1*). Drifting buoys, whose positions are determined by the French Service Argos aboard the NOAA spacecraft, transmit in situ SST measurements to NOAA polar-orbiting satellites and provide the data used to ensure MCSST accuracy. Separate time series are maintained for each buoy. During 1984 some 25 to 50 drifting buoys have been reporting through Argos into the World Meteorological Organization's Global Telecommunications System (GTS). They favor Earth's southern oceans; however, fixed buoys off the coasts of North America yield similar statistics. The system has provisions to accommodate adjustment for possible bias between sensors on successive NOAA operational satellites, and it will also selectively identify errors from buoy data transmission or from buoy and sensor failures that occasionally come through GTS. Monthly statistics from matchups of satellite MCSST data and SST data from drifting buoys scattered over the world ocean are shown in Fig. 1 for daytime and nighttime (*1*). Note the large bias error introduced by the eruption of the Mexican volcano El Chichón and the subsequent return to normal as the atmosphere cleared.

The dust veil from the April 1982 eruption of El Chichón had a temporary but marked effect on the ability of the NOAA-7 satellite's AVHRR to monitor SST. Micrometer- and submicrometer-sized particles of sulfuric acid injected into the stratosphere attenuated the radiation from Earth, causing a negative offset (bias) in NOAA's operationally recorded SST's. This offset, obtained by subtracting the ship-only SST analysis (National Weather Service) for each month from the satellite-only SST analysis, has been used to monitor the evolution and dispersion of the aerosol cloud (*3*). Latitudinal profiles of zonal averages of these monthly differences have been constructed from the 1982–83 data to monitor dispersion of the volcanic aerosol as it spread rapidly northward during November and December 1982 and into spring 1983. In the time plot shown in Fig. 2, each latitudinal average has been weighted by the decreasing proportionate area it represents from equator to pole. Furthermore, since the SST's are obtained only over water, it is assumed that the aerosol biases measured represent the bias for each entire latitudinal band. The temporal latitudinal plot shows results beginning with the first MCSST data in November 1981, although rigorous ship-only analyses were not available until 1982. The effect of the April eruption is obvious in Fig. 2. The aerosol at high latitudes in the Northern Hemisphere before the El Chichón eruption is believed to have come from the so-called mystery cloud that was being tracked by high-flying aircraft until El Chichón's contribution to the atmosphere overwhelmed the signal.

Three selected monthly mean charts of SST for the southeastern Pacific Ocean are presented together with climatological data in Fig. 3. Retrievals of MCSST's are made pass by pass from 4-km–resolution NOAA-AVHRR data and collected into a 2.5° latitude and longitude grid. Data for the month, both daytime and night-

H. Yates is director, A. Strong is a physical scientist, D. McGinnis is a hydrologist, and D. Tarpley is a physical scientist at the Office of Research and Applications, National Environmental Satellite, Data, and Information Service, NOAA, Washington, DC 20233.

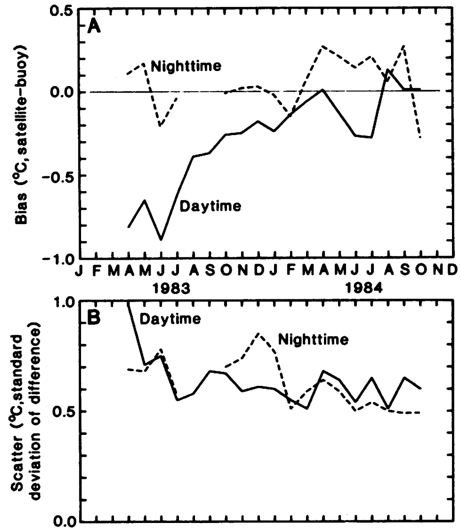

Fig. 1. Monthly mean biases (A) and scatter (B) for MCSST match-ups with drifting buoy SST's for 1983 and 1984. A 2-month gap in nighttime data during August and September 1983 resulted from electrical interference on the NOAA-7 spacecraft (*1*).

time, are then averaged into the NESDIS monthly mean MCSST field. Figure 3 is produced from an analysis of this field. The December charts for 1982, 1983, and 1984 show marked differences in the eastern tropical Pacific Ocean that graphically present the SST changes wrought by the strong 1982–83 El Niño (*4*).

In the eastern equatorial Pacific there appears annually a relatively cool tongue of water that is due to equatorial upwelling and the westward-flowing South Equatorial Current. The SST patterns associated with these annual cycles are monitored by the NOAA polar-orbiting satellites. Since the equatorial currents and upwelling are wind-forced, the SST patterns derived from satellites can be used to verify predicted SST patterns from numerical ocean circulation models. Although atmospheric models have been in use for several decades for weather prediction, global ocean circulation models are only beginning to be used to predict the oceanic response (*5*). One of the SST patterns that has been compared in both satellite measurements and numerical models is associated with equatorial long waves. These long waves (*5*) form north of the equator and propagate westward at about 40 km/day (*6*). An example of the SST pattern and associated long waves is shown in Fig. 4 for 8 November 1983, immediately following the 1982–83 El Niño event. During El Niño events the trade winds relax and the upwelling and South Equatorial Current become weak. Consequently, the long wave patterns are absent in the satellite-derived SST measurements.

The surface waters of the ocean vary markedly in color depending on the matter—plankton, silt, and pollutants—suspended in them. The Sargasso Sea and most tropical deep-ocean waters are a beautiful azure blue because they contain no plankton or sediment and the color is determined by the optical properties of the water alone. The waters of the North Atlantic are green because they are rich in phytoplankton, the tiny plants that grow where sufficient nutrients and light are present. They contain chlorophyll and function much as do their terrestrial cousins in that they scatter back predominantly green and infrared light. These aquatic plants use primarily blue light for driving their photosynthetic growth mechanisms. Figure 5 shows the spectral distribution of light scattered back from the ocean for four different concentrations of chlorophyll a. The first is relatively clear water, the last is "pea soup" water.

An interesting ocean color pattern between the mouth of the Rio de la Plata and the Falkland Islands is shown in Fig. 6. This image was produced from the coastal zone color scanner (CZCS) carried on the NASA Nimbus-7 research satellite, launched in 1978 and still producing useful data. The image is a computer-generated, color-coded map of the concentrations of chlorophyll pigments contained by phytoplankton. Additional information can be attained from the CZCS that is indicative of water turbidity and the amount of suspended matter in the surface layer (*7*). The processed image depicts the distribution of phytoplankton pigments associated with the confluence of two major current systems in the western South Atlantic. At the north is the warm Brazil Current flowing to the south at 1 to 2 knots. The waters associated with this current system originated with the South Equatorial Current and are poor in nutrients, resulting in very low biological productivity. Flowing from the south is the cold Falkland Current; these nutrient-rich waters support high rates of productivity, and concentrations reached 1.5 to 3.0 mg/m^3 in this case. Upon meeting, these two currents swing to the east, forming the South Atlantic Current.

Ocean color measurements have proven useful in locating good fishing grounds (*8*), as phytoplankton are the base of the food chain. The color patterns are also valuable indicators of ocean currents.

Hydrology

Satellites are providing data on snow cover, river and sea ice extent, and flood inundation. Regional snow cover is particularly important for predicting the runoff during the spring thaw and global-scale extent for climate monitoring.

Images obtained by the Geostationary Operational Environmental Satellite (GOES) are being used to monitor river basin snow cover for selected watersheds throughout the western United States and Canada (*9*). Twenty-eight basins, varying in size from 3,400 to 65,000 km^2 (Fig. 7) were monitored at NESDIS in Suitland, Maryland, from 1973 to 1980. Since 1980 the program has been decentralized and transferred to regional NESDIS offices as well as to primary users. Basins in the Rocky Mountains and Nevada (Nos. 12, 16 to 26, and 29 in Fig. 7) are being mapped from the NESDIS office in Kansas City; basins in the Pacific Northwest (Nos. 1 to 11) are monitored from the NESDIS office in San Francisco. Responsibility for monitoring basins in Arizona, California, and New Brunswick has been taken over by the Salt River Project, Sierra Hydrotech, Inc., and the Canadian Atmospheric Environment Service, respectively.

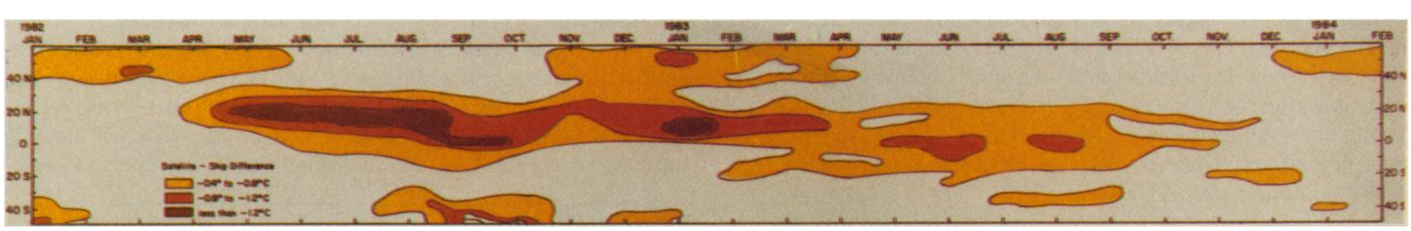

Fig. 2. Time plot of NOAA's MCSST offset in derived SST's by 2.5° latitudinal bands due to El Chichón aerosol beginning April 1982. SST differences are calculated by using satellite and ship monthly mean fields.

River basin snow maps are used by numerous federal, state, and local governmental agencies as well as public power utilities. The data are used in Arizona and Wyoming to aid in dam and reservoir operations. In the Pacific Northwest and New Brunswick, the snow cover data are used to calibrate runoff models. Existing snowmelt-runoff models (SRM's) for mountain basins have been modified to accept satellite data, thereby permitting application of SRM's in larger basins (*10, 11*). These models are designed to simulate and forecast daily streamflow in basins where snowmelt is a major contributor to runoff. In California, Nevada, and Montana the data are used for preparing seasonal water supply forecasts. Several analytical methods are available when using GOES data for snow mapping. In the simplest, an optical transfer device is used to magnify and rectify the GOES images until it overlies a standard hydrologic basin map. The snow line can then be transferred from image to map. The second method involves the use of computer-interactive systems to display the image data on a video screen. A joystick cursor or data tablet is then used to trace the snow line onto the image data. The final method involves use of mainframe computers to determine snow cover on a pixel basis. This involves thresholding each pixel according to terrain type and solar illumination angles. All three techniques can be used at NESDIS depending on basin characteristics and equipment availability.

The NESDIS has prepared the Northern Hemisphere weekly snow and ice cover chart (*12*). These charts show the areal extent and brightness of continental snow cover but do not indicate snow depth. The analysis is based on NESDIS satellite imagery, and the snow line represents the latest cloud-free image of that particular area of the world. The Northern Hemisphere snow cover charts have been digitized and stored on computer tape (*13*). Monthly, anomaly, frequency, and climatological snow cover maps can be created from the digitized data. In addition, continental or regional snow cover area can be calculated over a long time series, as shown in Fig. 8 for North American winter snow cover.

Although construction of flood-preventing structures has helped to protect lives and reduce losses, flood damage in the United States often exceeds $1 billion annually. Economics dictates that engineers and government officials be given improved information on the location of flood hazard areas and assessments of areas of inundation when floods occur. Satellites are a source of this information and have been used in research studies for the 1973 Mississippi River floods (*14*), the 1978 Kentucky River floods (*15*), and the Red River of the North floods of the same year (*16*). In each case the flooded areas showed up best in nighttime thermal infrared imagery owing to high temperature contrasts between land and water. Operational monitoring of flood extent through the use of NESDIS satellite data was done in support of National Weather Service river forecast centers during the Illinois River flood of December 1982 and the Pearl River floods of April 1983.

The watershed of the Red River of the North includes the northeastern corner of South Dakota, eastern North Dakota, northwestern Minnesota, and two small areas in Manitoba. Much of the basin is flat, causing flood waters to spread overland for many miles after even small rises of the river. Spring floods in 1978 resulted in record, or near-record, water levels in many areas (*17*). Figure 9A shows the flooded areas, which have been identified and transferred to a map of the region in Fig. 9B. Planimetric measurements of the

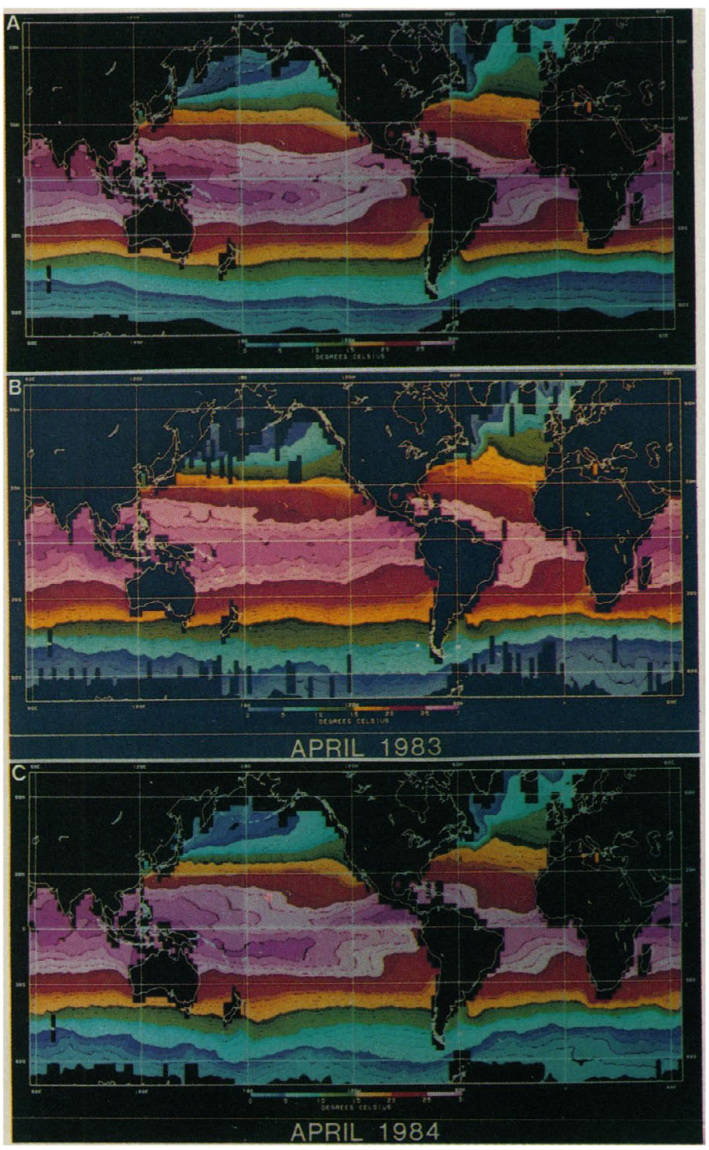

Fig. 3. Monthly mean MCSST fields produced at a 2.5° latitude and longitude grid: (A) climatology, (B) April 1983, and (C) April 1984. The effects of the 1982–83 record El Niño are captured in (B).

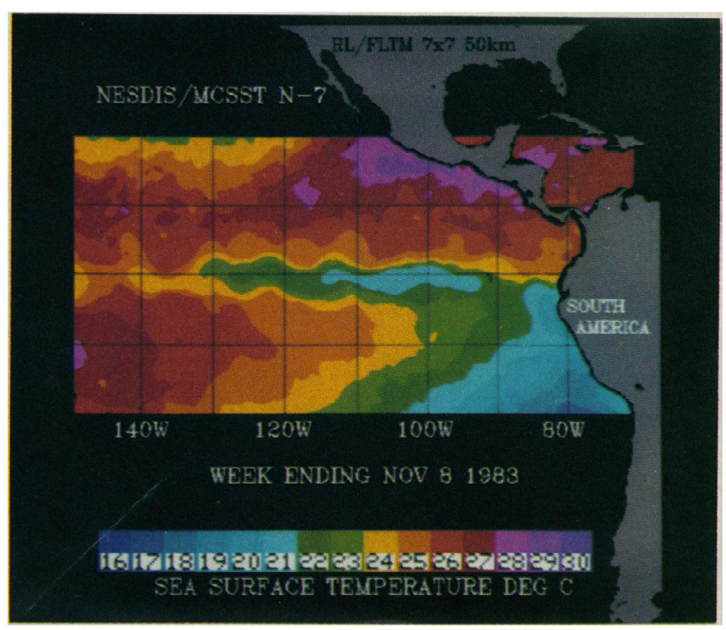

Fig. 4. Satellite-derived, color-coded SST field for the week ending 8 November 1983 in the eastern equatorial Pacific. The cool tongue of water along the equator is associated with upwelling and the westward-flowing South Equatorial Current.

inundated area follow the expected and observed trend of the discharge hydrograph recorded on the streamflow gauge at Drayton, North Dakota. The maximum stage at Drayton occurred on 16 April (fourth highest on record, or 20-year recurrence interval) and coincided with the greatest areal extent of the flood mapped from satellite imagery.

NOAA AVHRR infrared data can be used to identify areas of flooding in the case of large floods on large rivers. Furthermore, computer printouts and programs can be used to provide quick approximations of the total areal extent of a flood for disaster planning and relief service efforts.

In addition to monitoring floods, satellite data are used routinely to detect and locate ice cover and ice dams on a number of North American rivers. The dynamics of river ice are important because of the problems the ice creates for hydropower stations, bridge piers, and ship navigation. In addition, when the ice breaks up it can form a dam, posing a flood threat to nearby communities. McGinnis and Schneider (*18*) used Landsat and GOES imagery to detect and monitor ice jams in the Ottawa River. Fourteen distinct ice-covered reaches on the Ottawa River were located and identified on GOES imagery on 4 April 1976 (Fig. 10A). Man-made dams are partly responsible for the persistence of ice in five of the reaches. Sharp river bends account for two ice-covered segments, and branching of the main channel by islands contributes to the presence of ice in four other reaches. The profusion of ice in the downstream portion of the river may be attributable to the reduced slope of the river bottom as it approaches its confluence with the Saint Lawrence River. In contrast, the presence of rapids may explain the large ice-free stretch between the two most upstream reaches. As can be seen on the GOES image of 14 April (Fig. 10B), only three of the original ice reaches remained at the end of the 10-day study period.

This case study demonstrates that daily monitoring of changes in river ice can be effectively accomplished from geostationary satellites. The distortion in GOES imagery limits its usefulness to latitudes between 50°N and 50°S and to rivers at least 2 km wide. This precludes monitoring many subarctic rivers where ice is a problem, but polar-orbiting satellites could be used for these areas.

Currently, satellite-derived precipitation estimates and 3-hour precipitation trends for convective systems (*19*), extratropical cyclones (*20*), and tropical cyclones (*21*) are computed on the NESDIS interactive flash flood analyzer and transmitted to National Weather Service forecast offices, National Weather Service offices, and river forecast centers. These estimates and trends aid hydrologists and meteorologists in their evaluation of heavy precipitation events. The West Gulf River Forecast Center (Fort Worth, Texas) recently developed the capability of using satellite point-rainfall estimates from NESDIS for river predictions.

Agriculture

Weather is the most important and variable determinant of year-to-year changes in agricultural production. Forecasting of both domestic and foreign commodity production relies on routine weather observations reported by the global weather communications networks. The weather observations are used in numerical models that involve daily increments and provide estimates of soil moisture, crop yield, and crop stress. The data are also combined

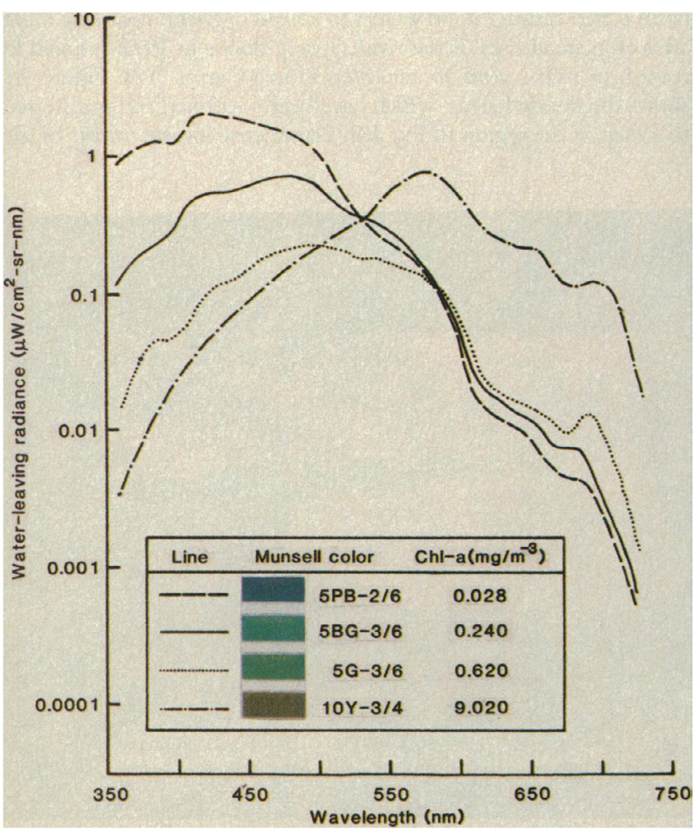

Fig. 5. Spectral distribution of light scattered back from the ocean for four different concentrations of chlorophyll a measured at the water surface. Note the reversal that occurs between 500 and 550 nm that becomes most marked when comparing extremely high with low values of pigment.

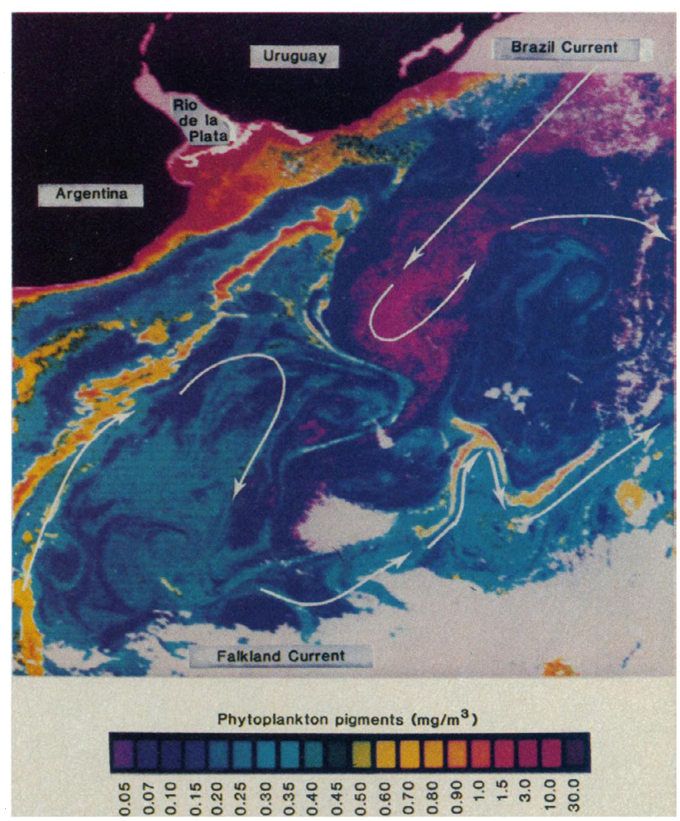

Fig. 6. Color-coded maps of phytoplankton pigment concentrations acquired off the coast of Argentina and Uruguay from Nimbus-7 CZCS imagery on 10 December 1978. In this presentation, land is black and clouds are white.

with other information by analysts, who then make qualitative estimates of agricultural conditions. The accuracy of the forecasts is reduced when weather observations are sparse or are not received in a timely manner. In many countries of agricultural importance, reported meteorological observations are not adequate for agricultural monitoring. Meteorological quantities that are needed for crop models and that can be estimated from satellite data include precipitation, daily temperature extremes, canopy temperature, insolation, and snow cover. These quantities are used in soil moisture and crop yield models, crop calendars, and, in the case of snow cover, winterkill estimates. They are also used to provide early warning of damaging situations such as drought and freeze events (*22–24*). In addition, there is a direct measure of the extent and condition of green vegetation, called a "vegetation index," that is derivable from satellite observations.

Algorithms to produce these quantities from operationally available satellite data have been developed. The satellite-derived quantities are blended with conventional observations, where possible, to provide a product that contains ground data where it is available and with satellite estimates filling in the gaps.

The distribution of precipitation at the surface is highly structured in space and time. It is influenced by small-scale convective elements within a large cloud system, orographic effects, atmospheric moisture availability, and wind conditions. Significant differences in rainfall are seen over distances of a few tens of kilometers in large-scale cyclonic frontal-type systems and over much smaller distances for showers and thunderstorms. Synoptic reporting stations are too widely spaced to adequately represent the distribution of rainfall at the resolution needed for agricultural monitoring. In agriculturally important areas of the Soviet Union, southeastern Brazil, and Argentina, the distance between rain-gauge reports ranges from 175

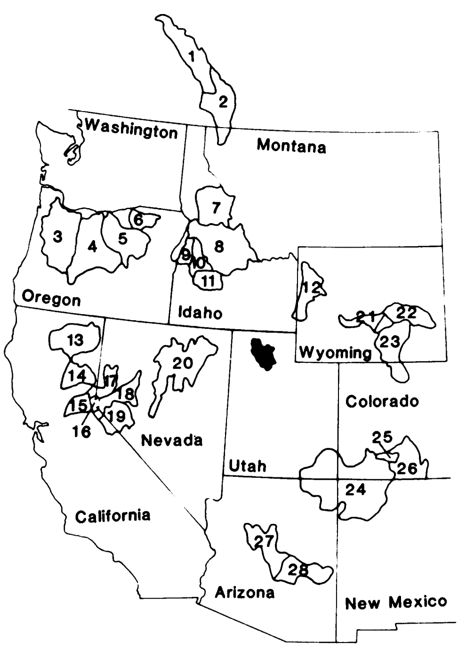

Fig. 7. River basins for NESDIS operational snow-mapping program.

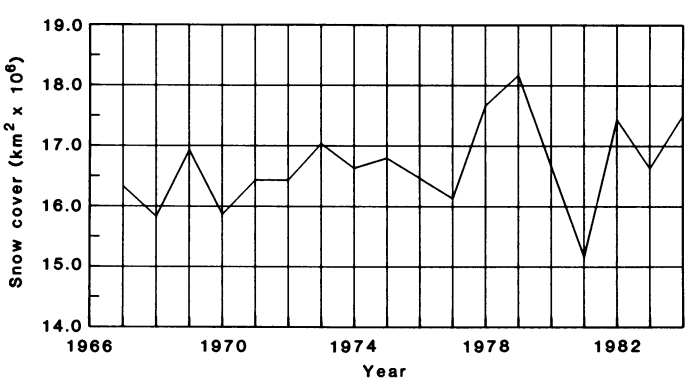

Fig. 8. North American winter snow cover, 1967 to 1983. Values are for December through February.

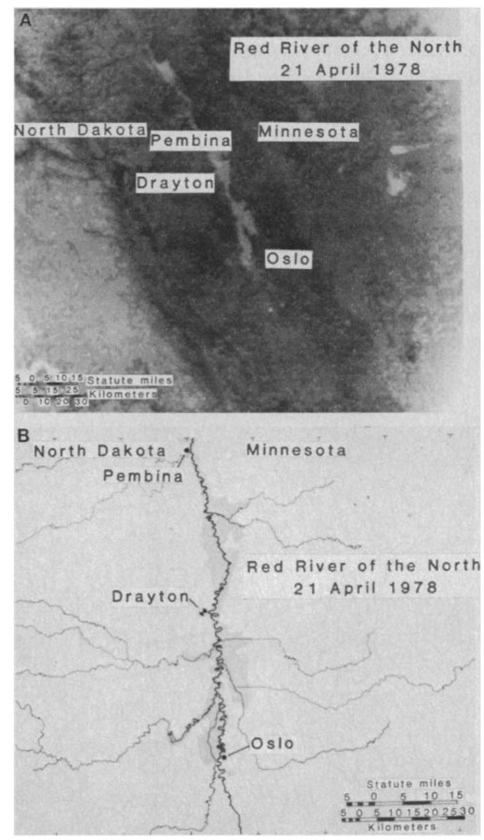

Fig. 9. (A) Rectified NOAA-5 VHRR infrared image (21 April 1978) of the Red River of the North showing flooding (light shades) on downstream areas. (B) Flood inundation map derived from the image in (A) for 21 April 1978.

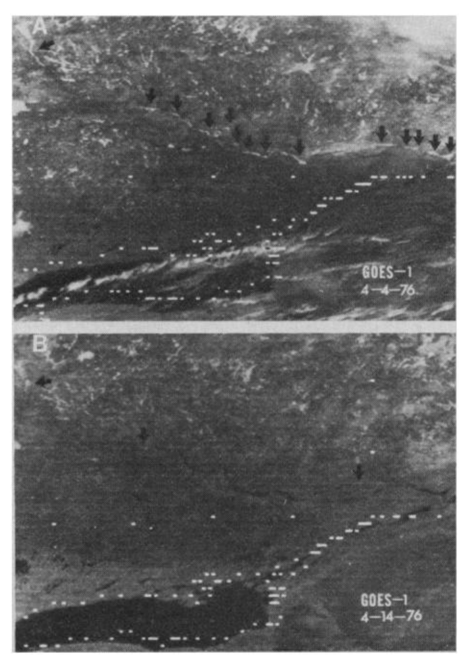

Fig. 10. (A) Ice-congested areas on the Ottawa River, 4 April 1976, as seen from GOES-1. (B) Ottawa River 10 days later, showing clearance of most of the ice congestion.

to 300 km. Heavy convective cells producing significant rain can pass unreported between synoptic stations. The U.S. Department of Agriculture crop forecasting grid (for foreign countries) has a spacing of 40 km, so there is a clear need for supplementary precipitation data.

The use of operationally available visible and infrared satellite data alone to estimate rainfall amount and distribution is not likely to be any better than synoptic rain-gauge data, except perhaps in areas where synoptic data are very sparse. The conditions that determine rainfall amount are correlated with cloud patterns and temperatures seen in the satellite data, but the correlation is not strong enough to allow accurate estimates. What can be done is to use satellite data to provide information on what happens between reporting synoptic stations. The satellite imagery and satellite precipitation estimates can be used to do a better spatial analysis of ground station precipitation reports.

Precipitation techniques have been developed for polar-orbiter and geostationary satellite data. For the Western Hemisphere, geostationary satellites are the data source because of the advantage of hourly observations. Geostationary data are used with a cloud-history precipitation algorithm (*25*). The cloud history technique allows the life cycle of a cloud to be tracked and rainfall estimated according to the size, altitude, and growth rate of the cloud. This technique was developed for convective cells and may not work as well with large-scale synoptic precipitation.

A method called cloud indexing is used to estimate precipitation from polar-orbiter data. This technique can be applied with only two observations per day from the polar orbiter, whereas cloud history methods require frequent observations. Cloud index methods have been developed by following two slightly different approaches (*26–29*), but all assign an index to clouds on the basis of cloud type, cloud amount, or cloud temperature and use the index in an empirical equation to estimate rain rate.

Current operational crop and soil moisture models require daily maximum and minimum shelter temperature and dew point temperature or relative humidity. These quantities are used in the models because they are conventionally observed. Canopy temperature may be more directly related to crop condition, but it is not routinely measured. The temperature of the radiating surface, or skin temperature, is routinely derived from satellite data and is a quantity that would be equal to canopy temperature if the sensor field of view were filled with the vegetated surface. Bare soil, water, and differing plant species within a field of view complicate the relation of skin temperature to canopy temperature.

Shelter temperature is a difficult quantity to estimate from satellites because no sensor responds to air temperature just within

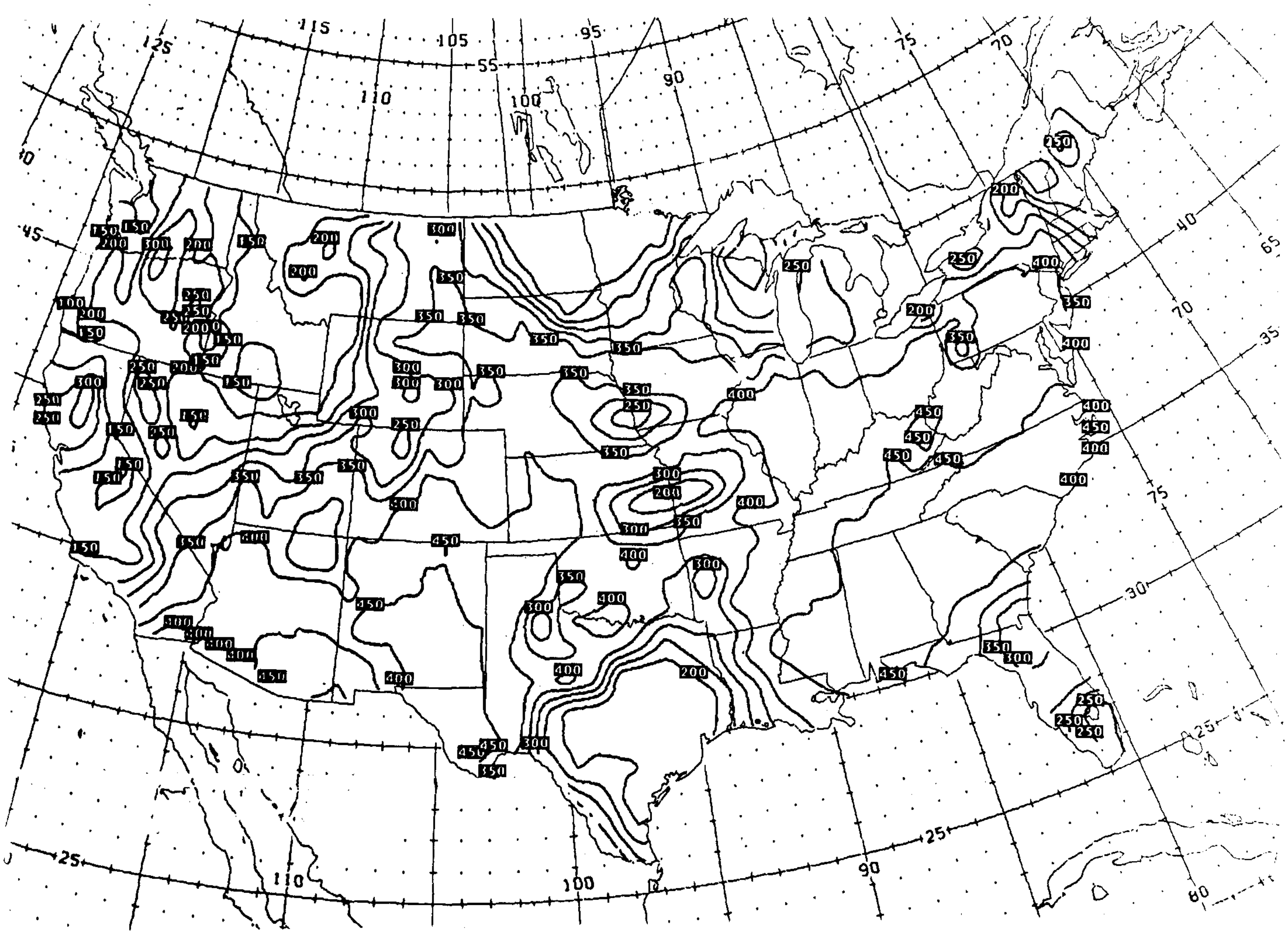

Fig. 11. Daily total insolation map made from GOES data on 13 March 1983. Units are langleys and the contour interval is 50 langleys. The areas with reduced insolation, such as Texas, the central and northern Great Plains, and the Pacific Coast states, were cloud-covered through the day.

the boundary layer, much less within a few feet of the surface. The TIROS Operational Vertical Sounder (TOVS) is the instrument used to estimate shelter temperature because it has thermal window channels and bands responding to radiation from the lower atmosphere. TOVS provides skin temperature and temperature profiles of the lower atmosphere that can be extrapolated to shelter level, provided that the temperature structure within the boundary layer is regular and no inversion occurs.

Regression techniques have been developed to estimate shelter temperature from satellite soundings and radiances (*29*) and to estimate daily maximum and minimum from shelter temperatures at a specific time. These regression methods are applied to NESDIS satellite temperature retrievals on a daily schedule, and daily shelter maximum and minimum temperatures are estimated. The greater errors found in winter are caused by the frequent occurrence of temperature inversions at the surface. Since there is no information in the satellite data about the detailed structure of the lowest few hundred meters of the atmosphere, inaccuracy caused by inversions will be difficult to remove. Other errors are introduced by the inability of the operational sounding processing to correctly identify the cloud condition in a sounded area, particularly during winter when the ground and clouds have similar temperatures and reflectivities, thus making difficult the separation of cloud-free and cloud-covered regions.

Insolation is the primary energy source for growing crops, and it is used in numerical models for estimating crop yield, evaporation, and soil moisture. The amount of solar radiation reaching the surface is determined by the transmittance of the atmosphere, and clouds are the most important factor affecting transmittance. Under overcast conditions, up to 70 percent of incident solar radiation may be reflected to space and another 10 to 15 percent absorbed. The satellite directly observes the reflected component of the incident radiation, so satellite measurements in the visible part of the spectrum are directly related to insolation at the surface. GOES is the preferred data source for satellite estimates of insolation because its repeated observations throughout the day allow tracking of changing cloud conditions. A method has been developed that uses hourly GOES visible data to estimate hourly insolation (*30, 31*). The technique involves regression against observed target brightness as measured by GOES and the known brightness of the target under clear conditions. The difference between these two quantities is a measure of cloudiness. Hourly estimates are summed to give daily total insolation, which is the measure used in agricultural models.

Daily insolation estimates are being made and archived for all of the United States and for agriculturally important areas in Mexico and South America. The estimates are made for 50-km targets centered at the intersection of 1° interval lines of latitude and longitude. Hourly estimates are made from six (western United States and South America) and seven (eastern United States and Mexico) hourly GOES images distributed about 1200 hours local time. The hourly estimates are interpolated to fill in missing hours and the values are summed to provide a daily total. Figure 11 shows the daily estimates for 13 March 1983. Areas of low insolation, such as the one in Texas, correspond to persistent cloud cover throughout the day.

When the ground is snow-covered, the algorithm underestimates insolation because bright snow is mistaken for clouds. Other sources of error are mislocation of satellite data, cloud changes that occur when data are unavailable or not used, and difficulties in maintaining accurate scene brightness index under cloud-free conditions.

The visible and near-infrared bands on the AVHRR allow monitoring the greenness or vigor of vegetation on a global scale (*32–35*). AVHRR channel 1 observes in the 0.55- to 0.68-μm band and channel 2 covers 0.73 to 1.1 μm. Green vegetation has a reflectance of about 20 percent in the channel 1 spectral region, but up to 60 percent in channel 2. Other features viewed from space, such as bare ground, water, snow, and clouds, have similar reflectances in the two bands or a greater reflectance in channel 1 than in channel 2. Various mathematical combinations of channels 1 and 2 radiances are correlated with the density and greenness of vegetation and are referred to as vegetation indices. Initial studies of vegetation from satellite data made use of multispectral scanner bands 5 and 7 on Landsat, which have spectral bands similar to channels 1 and 2, respectively, but 80-m rather than 1- or 4-km resolution. The advantage of using NOAA satellites to monitor vegetation is that the repeat cycle is daily in contrast to 18 days with Landsat. The most commonly used indices are the simple vegetation index, VI, and the normalized vegetation index, NVI, which are computed from the equations $VI = Ch_2 - Ch_1$ and $NVI = (Ch_2 - Ch_1)/(Ch_2 + Ch_1)$. The NVI is preferred because it partially compensates for changing illumination conditions, surface slope, and viewing aspect.

Figure 12 shows a typical polar stereographic image of the Northern Hemisphere NVI for the week of 23 August 1982. These images are made from 4-km data from channels 1 and 2 that are mapped each day into 1024 by 1024 polar stereographic arrays for the Northern and Southern hemispheres. Resolution in the mapped arrays ranges from 15 km at the equator to 30 km at the poles. The mapping algorithm maps all pixels, replacing previously mapped pixel values with the latest one. This procedure is randomized somewhat by day-to-day jitter introduced by a ±10-km error in Earth location accuracy.

Recent research has demonstrated the utility of operational satellite data in monitoring the condition and extent of forests, rangeland, and agricultural areas.

Fig. 12. NOAA-7 Northern Hemisphere vegetation index map for 23 to 29 August 1982. Clouds have been mostly eliminated from this map by compositing daily maps for the 7-day period and retaining at each array location the "greenest," and therefore clearest, observation over the 7 days. Such maps are produced weekly at NESDIS for both hemispheres.

REFERENCES AND NOTES

1. A. E. Strong and E. P. McClain, *Bull. Am. Meteorol. Soc.* **65**, 138 (1984).
2. A. E. Strong, in preparation.
3. ———, *Geofis. Int.* **23**, 129 (1984).
4. E. M. Rasmusson and J. M. Wallace, *Science* **222**, 1195 (1983).
5. S. G. H. Philander, *J. Geophys. Res.* **83**, 3679 (1978).
6. R. Legeckis, W. Pichel, G. Nesterczuk, *Bull. Am. Meteorol. Soc.* **64**, 133 (1983).
7. H. R. Gordon *et al.*, *Appl. Opt.* **22**, 20 (1983).
8. R. M. Laurs, P. C. Fiedler, D. R. Montgomery, *Deep Sea Res.* **31**, 1085 (1984).
9. S. R. Schneider, *NASA Tech. Pap.* **1827** (1981).
10. A. Rango and J. Martinec, *Nordic Hydrol.* **10**, 225 (1979).
11. J. Martinec, A. Rango, E. Major, *NASA Ref. Publ.* 1100 (1983).
12. M. Matson and D. R. Wiesnet, *Nature (London)* **289**, 451 (1981).
13. K. F. Dewey and R. Heim, Jr., *NOAA Tech. Rep. NESS-87* (1981).
14. D. R. Wiesnet, D. F. McGinnis, J. A. Pritchard, *Wat. Resour. Bull.* 10, 1040 (1974).
15. C. P. Berg and D. F. McGinnis, paper presented at the 46th Annual Meeting of the American Society of Photogrammetry, St. Louis, MO (1980).
16. C. P. Berg *et al.*, in *Satellite Hydrology*, M. Deutsch, D. R. Weisnet, A. Rango, Eds. (American Water Resources Association, Sioux Falls, SD, 1981), pp. 309–315.
17. *Red River of the North Post Flood Report 1978* (U.S. Army Corps of Engineers, St. Paul, MN, 1979).
18. D. F. McGinnis and S. R. Schneider, *Photogramm. Eng. Remote Sens.* **44** (No. 1), 57 (1978).
19. R. A. Scofield, paper presented at the Tenth Conference on Weather Forecasting and Analysis, Clearwater Beach, FL (25–29 June 1984).
20. ——— and L. E. Spayd, Jr., *NOAA Tech. Memo. NESDIS 8* (1984).
21. L. E. Spayd, Jr., and R. A. Scofield, *NOAA Tech. Memo. NESDIS 5* (1984).
22. J. F. Bartholic and R. A. Sutherland, *Proc. Fla. State Hort. Soc.* **91**, 334 (1978).
23. J. D. Martsolf, paper presented at the Conference on Cooperative Climate, Tallahassee, FL (1983).
24. ———, *Citrus Ind.* **64**, 24 (1983).
25. C. R. Griffith *et al.*, *Mon. Weather Rev.* **106**, 1153 (1978).
26. L. J. Heitkemper, paper presented at the International Conference on Interactive Information and Processing Systems for Meteorology, Oceanography, and Hydrology, Los Angeles (7 to 11 January 1985).
27. J. F. Moses, paper presented at the International Conference on Interactive Information and Processing Systems for Meteorology, Oceanography, and Hydrology, Los Angeles (7 to 11 January 1984).
28. E. C. Barrett and D. W. Martin, *The Use of Satellite Data in Rainfall Monitoring* (Academic Press, New York, 1981).
29. P. A. Davis and J. D. Tarpley, *J. Clim. Appl. Meteorol.* **22**, 369 (1983).
30. J. D. Tarpley, *J. Appl. Meteorol.* **18**, 1172 (1979).
31. C. G. Justus and J. D. Tarpley, paper presented at the American Meteorological Society Atmospheric Radiation Conference, Baltimore (1983).
32. C. J. Tucker, J. A. Gatlin, S. R. Schneider, *Photogramm. Eng. Remote Sens.* **50**, 53 (1984).
33. J. D. Tarpley, S. R. Schneider, R. L. Money, *J. Clim. Appl. Meteorol.* **23**, 491 (1984).
34. S. R. Schneider and D. F. McGinnis, Jr., paper presented at the Eighth International Symposium on Machine Processing of Remotely Sensed Data, Purdue University (1982).
35. C. J. Tucker, J. R. G. Townshend, T. E. Goff, *Science* **227**, 369 (1985).

Research Articles

The Intervening Sequence RNA of *Tetrahymena* Is an Enzyme

ARTHUR J. ZAUG AND THOMAS R. CECH

A shortened form of the self-splicing ribosomal RNA (rRNA) intervening sequence of *Tetrahymena thermophila* acts as an enzyme in vitro. The enzyme catalyzes the cleavage and rejoining of oligonucleotide substrates in a sequence-dependent manner with $K_m = 42$ μM and $k_{cat} = 2$ min^{-1}. The reaction mechanism resembles that of rRNA precursor self-splicing. With pentacytidylic acid as the substrate, successive cleavage and rejoining reactions lead to the synthesis of polycytidylic acid. Thus, the RNA molecule can act as an RNA polymerase, differing from the protein enzyme in that it uses an internal rather than an external template. At *p*H 9, the same RNA enzyme has activity as a sequence-specific ribonuclease.

IN RNA SELF-SPLICING, THE FOLDED STRUCTURE OF AN RNA molecule mediates specific cleavage-ligation reactions (*1–5*). Self-splicing exemplifies intramolecular catalysis (*6*) in that the reactions are accelerated many orders of magnitude beyond the basal chemical rate (*7, 8*). The reactions are highly specific, as seen in the choice of a free guanosine nucleotide as a substrate in the self-splicing of the *Tetrahymena* ribosomal RNA precursor (pre-rRNA) and other RNA's containing group I intervening sequences (*1–3, 7*). Furthermore, the cleavage-ligation activity mediates a series of splicing, cyclization, and reverse cyclization reactions, suggesting that the active site is preserved in each reaction (*9, 10*). However, the RNA is cleaved and rejoined during self-splicing; because the RNA is not regenerated in its original form at the end of the reaction, it is not an enzyme. The RNA moiety of ribonuclease P, the enzyme responsible for cleaving transfer RNA (tRNA) precursors to generate the mature 5′ end of the tRNA, has been the only example of an RNA molecule that meets all criteria of an enzyme (*11–13*).

Following self-splicing of the *Tetrahymena* rRNA precursor, the excised IVS RNA (*14*) undergoes a series of RNA-mediated cyclization and site-specific hydrolysis reactions. The final product, the L − 19 IVS RNA, is a linear molecule that does not have the first 19 nucleotides of the original excised IVS RNA (*9*). We interpreted the lack of further reaction of the L − 19 species as an indication that all potential reaction sites on the molecule that could reach its active site (that is, intramolecular substrates) had been consumed; and we argued that the activity was probably unperturbed (*9*). We have now tested this by adding oligonucleotide substrates to the L − 19 IVS RNA. We find that each IVS RNA molecule can catalyze the cleavage and rejoining of many oligonucleotides. Thus, the L − 19 IVS RNA is a true enzyme. Although the enzyme can act on RNA molecules of large size and complex sequence, we have found that studies with simple oligoribonucleotides like pC_5 (pentacytidylic acid) have been most valuable in

Thomas R. Cech is a professor and Arthur J. Zaug is a research associate in the Department of Chemistry and Biochemistry, University of Colorado, Boulder, 80309-0215. Send correspondence to T.R.C.